Chinese Chemical Letters 34 (2023) 107718

Contents lists available at ScienceDirect

Chinese Chemical Letters

journal homepage: www.elsevier.com/locate/cclet

Complementary dual-doping of $LiNi_{0.8}Co_{0.1}Mn_{0.1}O_2$ cathode enhances ion-diffusion and stability for Li-ion batteries

Zhihong Wang[a,c], Huawei Zhu[a], Haifeng Yu[a], Tao Zhang[c], Yanjie Hu[a,b], Hao Jiang[a,b,*], Chunzhong Li[a,b,*]

[a] *Shanghai Engineering Research Center of Hierarchical Nanomaterials, School of Materials Science and Engineering, East China University of Science and Technology, Shanghai 200237, China*
[b] *Key Laboratory for Ultrafine Materials of Ministry of Education, School of Chemical Engineering, East China University of Science and Technology, Shanghai 200237, China*
[c] *State Key Lab of High Performance Ceramics and Superfine Microstructure, Shanghai Institute of Ceramics, Chinese Academy of Sciences, Shanghai 200050, China*

ARTICLE INFO

Article history:
Received 26 March 2022
Revised 25 July 2022
Accepted 30 July 2022
Available online 31 July 2022

Keywords:
$LiNi_{0.8}Co_{0.1}Mn_{0.1}O_2$
Dual-doping
High power
Cycling stability
Li-ion batteries

ABSTRACT

The Ni-rich $LiNi_{0.8}Co_{0.1}Mn_{0.1}O_2$ (NCM811) layered cathodes endow Li-ion batteries (LIBs) with high energy density. However, they usually suffer from limited ion-diffusion and structural instability during cycling. Although doping strategy can effectively alleviate these issues, the coupling effects of multi-element doping and the corresponding performance enhancement mechanism have been yet unclear. Here, we report a Zr/Ti dual-doped NCM811 cathode material (ZT-NCM811), in which Zr-ion is doped into both transition metal (TM) layers and lithium layers and Ti-ion is only distributed in TM layers. The dual-doping can effectively enhance crystal structure stability *via* inhibiting the lattice collapse along c-axis and decreasing the Li/Ni disorder. Meantime, the lattice oxygen escape is also greatly reduced due to the presence of stronger Zr-O and Ti-O bonds, further mitigating the crystal surface parasitic reactions with electrolyte. The resultant ZT-NCM811 exhibits high specific capacity of 124 mAh/g at even 10 C, much higher than undoped and single-doped NCM811, and a retention of 98.8% at 1 C after 100 cycles. The assembled ZT-NCM811/graphite full cell also delivers superior battery performances and durability.

The compelling demand for new energy vehicles with long driving range and fast-charging has promoted the innovation of advanced automotive lithium-ion batteries (LIBs) [1–3]. The cathode materials are the predominant limiting factor for the development of LIBs. Recently, Ni-rich layered oxide cathode materials have drawn great attention by virtue of their high discharge specific capacity (theoretical capacity of 274 mAh/g) and operation voltage [4,5]. Unfortunately, the structural instability and sluggish ion-diffusion limit its widespread commercial application [6]. Specifically, the anisotropic mechanical internal stress caused by abrupt shrinkage along c-axis during charging will lead to intergranular and intragranular microcracks, finally resulting in the disintegration of the secondary particles [4,7]. In addition, more serious Li/Ni disorder along with higher Ni content will limit the de-intercalation of lithium ions, triggering sluggish ion-diffusion [8]. Meanwhile, the electron migration between strong oxidizing Ni^{4+} and O^{2-} induces the oxygen gas release in lattice framework, which will accelerate the structure transformation from the layered phase to the electrochemically inactive rock salt phase [9,10]. Considering the microcrack generation and lattice structure evolution are the dominating factors resulted in the performance deterioration, it is essential to promote structure durability of Ni-rich cathode materials [11].

Integration of extraneous metal ions (Mo [12], Mg [13], Ti [14], Al [15], Zr [16], *etc.*) into the crystal structure has been proved to be a resultful method to address the aforementioned problems of the electrode materials. Nevertheless, single element doping strategy can only suppress cathode materials failure in specific aspect, for instance, lattice oxygen stability, ion-diffusion rate or layered structure strength. Hence, combining the respective function of different dopant, multielement doping is more promising to address above problems for the layered oxide materials at the same time [17–19]. Regrettably, introducing more than one dopant may generate elements redistribution and hierarchical structure even exhibiting pernicious functionalities in battery performance [18], and the doping mechanism of multielement doping strategy remains

* Corresponding authors.
E-mail addresses: jianghao@ecust.edu.cn (H. Jiang), czli@ecust.edu.cn (C. Li).

https://doi.org/10.1016/j.cclet.2022.07.061
1001-8417/

unclear and debatable. Therefore, it is momentous to propose a high-efficient strategy to achieve the homogeneous co-doping and conduct in-depth analysis of electrochemical enhancement mechanism for novel Ni-rich oxides.

In this work, the Zr/Ti dual-doped NCM811 with optimized lattice structure and electrochemical performance was synthesized successfully. Zr ions in Li slabs acted as pinning ions can inhibit the lattice collapse along the c-axis and alleviate the Li/Ni disorder [20–22]. Meanwhile, Zr ions and Ti ions doped in transition metal (TM) layers can enhance lattice oxygen stability during de-lithiation/lithiation in virtue of the high bonding energy. Benefitting from synergetic reinforcement of co-doping strategy, as-prepared ZT-NCM811 materials exhibit a capacity retention of 98.8% after 100 cycles at a current density of 1 C, and a high specific capacity of 124 mAh/g at even 10 C, which is much higher than that of the pristine sample (98 mAh/g at 10 C). The assembled ZT-NCM811/graphite pouch cell also delivers an outstanding cycling performance of 87.2% after 300 cycles at 1 C.

The NCM811 was obtained *via* a traditional lithiation sintering method employing $Ni_{0.8}Co_{0.1}Mn_{0.1}(OH)_2$ precursor (GEM Co., Ltd.) and $LiOH{\cdot}H_2O$ as raw materials. The $LiOH{\cdot}H_2O$ and $Ni_{0.8}Co_{0.1}Mn_{0.1}(OH)_2$ were mixing homogeneously with a molar percentage of 1.05:1, and next pre-calcined at 500 °C for 300 min and sintered at 750 °C for 900 min in the condition of pure oxygen. To prepare 0.5ZT-NCM811, 37.5 mg $ZrO(NO_3)_2$ and 3 g $Ni_{0.8}Co_{0.1}Mn_{0.1}(OH)_2$ was dispersed into 100 mL deionized water (DI) at the same time, marked as solution A. Meanwhile, 55 mg tetrabutyl titanate was added into 60 mL absolute ethanol and stirred adequately, marked as solution B. Peristaltic pump was used to pump solution B into solution A with a flow rate at 2 mL/min. The suspension liquid was heated at 80°C and vigorously stirred until DI was evaporated completely, and then the resulting precipitate was calcined at the same condition as NCM811. Analogously, the ZT-NCM811 with different doping contents were obtained *via* the identical method.

The crystallographic structural analysis of cathodes materials was conducted by X-ray diffraction (XRD, Bruker D8 Advance) adopting Cu Kα radiation operated at 40 kV with a scanning speed of 2°/min. The surface element compositions and valence were characterized by the X-ray photoelectron spectra (XPS, ESCA PHI500C) with Al Kα radiation ($h\nu = 1486.6$ eV). The morphologies of all the cathodes materials were researched *via* the field emission scanning electron microscopy (FESEM, GeminiSEM 500), and the cross section of the ZT-NCM811 was prepared by focused ion beam etching technique (TESCAN GALA 3). The hyperfine structure and elements distributions were analyzed *via* high-resolution transmission electron microscopy (FEI Talos F200X). The percentage of elements for all samples were acquired by inductively coupled plasma optical-emission spectrometer (Agilent 725). The *in situ* differential electrochemical mass spectrometry (DEMS) characterization was conducted on DEMS-QAS 100 (Linglu Instruments (Shanghai) Co., Ltd.), using Ar as the carrier gas and the flow rate of Ar was 0.9 mL/min.

The 2016 coin cells were assembled in a glove box (< 0.1 ppm for H_2O and O_2) with argon environment to evaluate the electrochemical properties of cathode materials. The active materials, poly(vinylidene fluoride) (PVDF), and carbon black (super-P) were blending at a mass ratio of 8:1:1 in moderate *N*-methyl-2-pyrrolidone (NMP), and then spread onto the Al foil with a loading of 1.5-2.0 mg/cm^2. The Lithium metal and polypropylene film (Celgard 2400) were used as counter electrode and separate, respectively. The electrolyte solution was 1.2 mol/L $LiPF_6$ dissolved in ethyl methyl carbonate (EMC) and ethylene carbonate (EC) (volume ratio = 7:3) with 2 wt% vinylene carbonates (VC). The pouch cell was assembled using commercial graphite as an anode. After stacking with monolayer anode, membrane and monolayer cathode, the pouch cell was packed through aluminum-plastic film and then injected with electrolyte. The LANDCT2001A test system was adopted to conduct the galvanostatic charge/discharge measurements. The electrochemical impedance spectra (EIS) and the cyclic voltammetry (CV) at different sweep rates were carried out through the Autolab PGSTAT302N and the EIS was tested from 10^5 Hz to 10^{-2} Hz at the voltage of 4.3 V. To analyze the structure and the dissolution of TM of cycled cathodes, the 2016 coin cells were disassembled in glove box. The electrode slices were washed by pure dimethyl carbonate (DMC), the Li anodes were dissolved in HNO_3 and dispersed by DI to a constant volume.

As the schematic representation of NCM811 construct design presented in Fig. 1a, Zr elements have thermodynamic substitution preference in both the transition metal layers and lithium layers, while Ti ions only distributed in (TM) layers. Benefiting from the duplex reinforcement of layer structure, ZT-NCM811 is expected to reach a best electrochemical performance. In order to select the appropriate doping content, the NCM811 with different amount of dopant were synthesized. As shown in Fig. S1 and Table S1 (Supporting information), the XRD Rietveld refinement and the corresponding results indicate that the doping of Zr and Ti does not affect the main structure of NCM811, ordered layer structure of all samples are well-maintained. However, the Li/Ni disorder of ZT-NCM811 increase with the increasement of doping content, which will degrade the rate performance of cathode materials [23,24]. Low doping concentration is most suitable for industrial production [17], hence, 0.5 mol% content of Zr and Ti (0.5ZT-NCM811) was chosen to further study and the ZT-NCM811 appeared in this article are all point to 0.5 mol% doping content.

In order to clarify the specific effect of Zr or Ti doping, Zr doping NCM811 (Zr-NCM811) and Ti doping NCM811 (Ti-NCM811) of 0.5mol% were synthesized. The XRD patterns of ZT-NCM811, Zr-NCM811, Ti-NCM811, NCM811 are displayed in Fig. 1b, all the peaks are indexed to the layered α-NaFeO2 structure with *R-3m* space group. Meanwhile, the distinct splitting of (006)/(102) and (018)/(110) peaks predicates the well-ordered layered structure [13,25]. The corresponding Rietveld refinement results, as shown in Tables S2 and S3 (Supporting information), indicate that the lattice parameters *a* and *c* and the unit volume increase slightly after Zr and Ti modification, which is mainly due to the larger ionic radius of Zr^{4+} (0.072 nm) and Ti^{4+} (0.061 nm) in comparison to Ni^{3+} (0.056 nm), Co^{3+} (0.055 nm) and Mn^{4+} (0.053 nm) [26,27]. The percentage of Zr^{4+} locates at Li site of Zr-NCM811, ZT-NCM811 are 0.22% and 0.23%, respectively, which is consistent with previous reports [20–22,26,28]. For the $Ni2p_{2/3}$ spectra (Fig. S2 in Supporting information), the characteristic peaks located at 854.6 and 855.8 eV illuminate the coexist of Ni^{2+} and Ni^{3+} in the cathode materials [13]. Interestingly, despite the increase of Ni^{2+}/Ni^{3+} ratio due to the charge compensation, the degree of Li/Ni disorder decreases after the doping of zirconium or titanium with 0.5 mol%, as shown in Fig. 1c, implying that the modulation of Zr and Ti content is extremely critical for reducing the Li/Ni disorder [12,29]. For O1s regions in Fig. 1d, the peaks at 528.9 and 531.4 eV represent the lattice oxygen and surface adsorbed species (LiOH or Li_2CO_3) [12,13]. For C1s spectra in Fig. S3 (Supporting information), the peaks at 289.7 and 284.8 eV are connected with Li_2CO_3 and adventitious carbon, respectively. ZT-NCM811 has the highest lattice oxygen content and minimum Li_2CO_3 content, indicating that surface residual lithium salt decrease through Zr and Ti doping. Meanwhile, Zr and Ti are doped in the form of 4 valence, as shown in Figs. 1e and f. The stronger Ti-O bonds and Zr-O bonds can robust the lattice oxygen and stabilize the host structure during electrochemical cycle process [30,31].

The element compositions of all the samples are investigated by inductively coupled plasma optical-emission spectrometer (ICP-OES), as displayed in Table S4 (Supporting information), and the

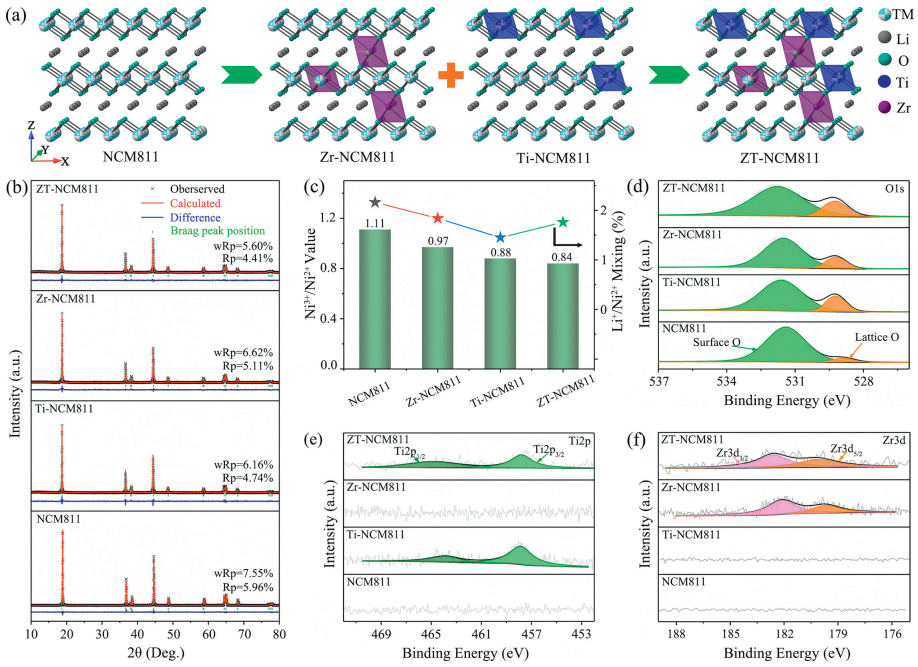

Fig. 1. (a) Schematic illustration of the crystal structure, (b) XRD Rietveld refinement, (c) cation mixing of Ni^{2+} in Li layer and ratio value of Ni^{3+}/Ni^{2+}, and (d) O 1s, (e) Ti 2p and (f) Zr 3d XPS spectra of the ZT-NCM811, Zr-NCM811, Ti-NCM811, NCM811.

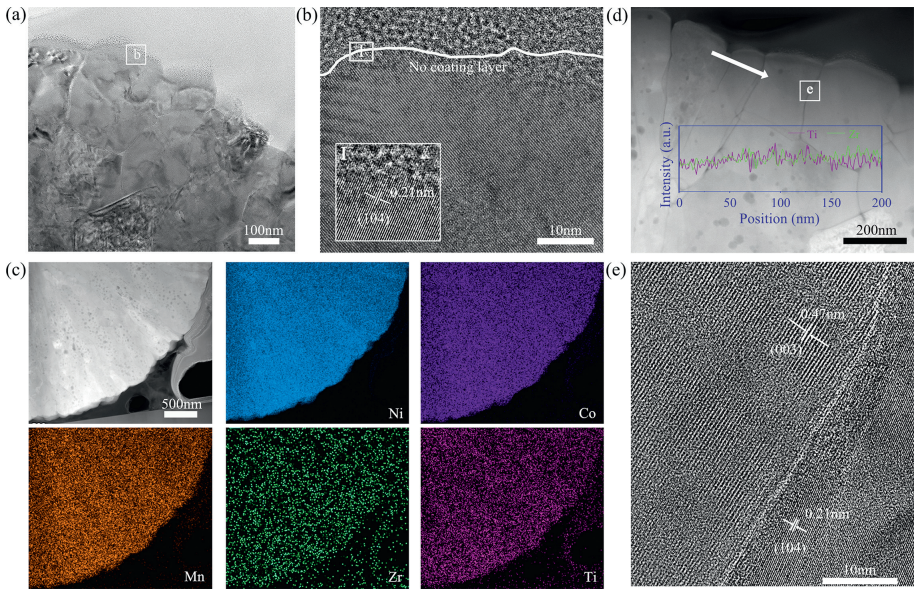

Fig. 2. (a) Low- and (b) high-resolution TEM images, (c) EDS elemental mappings, (d) STEM-HAADF image and corresponding EDS element line distribution of Zr (green line) and Ti (purple line), and (e) high-resolution TEM image between two primary particles of the ZT-NCM811.

doping content of Zr and Ti are consistent with feeding quantity. Furthermore, SEM and TEM characterization were further carried out to investigate the morphology of samples and the hyperfine distributions of Zr and Ti. Fig. S4 (Supporting information) is the SEM images of ZT-NCM811, Zr-NCM811, Ti-NCM811, NCM811. All materials have a spherical-like morphology consisted of similar primary particles without obvious difference on the surface. It is worth noting that there is no coating layer on the surface of ZT-NCM811, (Figs. 2a and b) implying all the Zr and Ti elements are doped into the lattice structure of NCM811. Meanwhile, the STEM-EDS mapping in Fig. 2c demonstrates the homogenous distribution of the Ni, Mn, Co and suggests that the Zr and Ti uniformly dope into the lattice of NCM811. Besides, there is no enrichment of Zr and Ti along the grain boundary (Fig. 2d), and the High-resolution TEM images shown in Fig. 2e further corroborates this point.

The fundamental electrochemical performance of as prepared cathodes was evaluated in coin cells within a voltage range of 2.7–4.3 V. As depicted in Fig. 3a, the ZT-NCM811 displays a comparatively higher ICE of 87% and the typical first charge/discharge curves of four samples are presented in Fig. S5 (Supporting information). Simultaneously, the rate capabilities and the capacity retention after 100 cycles at 1 C of the ZT-NCM811 were also displayed with NCM811, Zr-NCM811, Ti-NCM811 as references (Figs. 3b and c). Obviously, The ZT-NCM811 has the highest discharge capacity of 212 mAh/g at 0.1 C and 124 mAh/g at 10 C, superior to those of NCM811, Zr-NCM811 and Ti-NCM811, which results from removal of the residual lithium salts and the increased Ni^{2+} after Zr and Ti co-doping [30–32]. It is remarkable noted that ZT-NCM811 can deliver a capacity retention ratio of 98.8% after 100 cycles whilst the NCM811, Zr-NCM811, Ti-NCM811 only display a

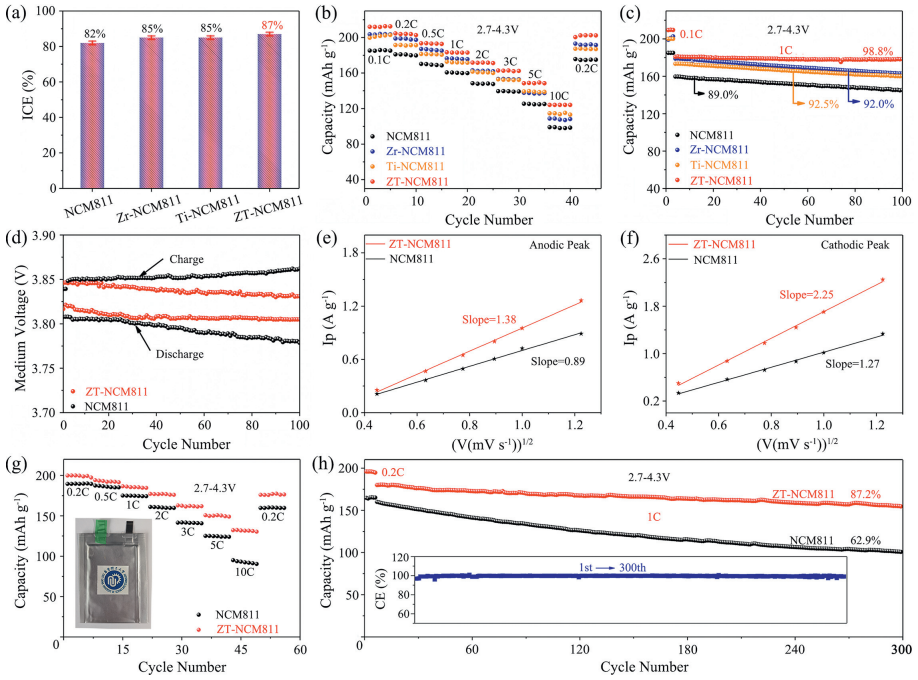

Fig. 3. (a) Initial Coulombic efficiency, (b) specific capacities at 0.1-10 C, (c) cyclic performance at 1 C of the ZT-NCM811, Zr-NCM811, Ti-NCM811 and NCM811. (d) Charge and discharge medium-voltage change during cycling, (e, f) linear relationship between the anodic/cathodic peak current (ip) and the square root of the scan rate (v1/2) for the ZT-NCM811 and NCM811. (g) Rate capability and (h) cycling stability with corresponding Coulombic efficiency of the ZT-NCM811/graphite and NCM811/graphite full cells.

capacity retention of 89.0%, 92.0%, 92.5%, respectively. To highlight the improvement performance of co-doping strategy, the medium dis/charge voltage evolution during cycling for the ZT-NCM811 and NCM811 are shown in Fig. 3d, the medium dis/charge voltage of ZT-NCM811 has no obvious change after 100 cycles, indicating less cathode-electrode polarization after co-doping [33], which is consistent with the initial three CV results (Fig. S6 in Supporting information). Besides, the linear relationship between the peak current (i_p) and square root of the scan rate ($v^{1/2}$) obtained from CV curves operating at various scan rates of 0.2, 0.4, 0.6, 0.8, 1 and 1.5 mV/s (Fig. S7 in Supporting information), respectively, confirms that a diffusion-controlled process of Li^+ transfer in ZT-NCM811 and NCM811. The larger slopes of ZT-NCM811 than that of NCM811 indicates the Li-ion diffusion kinetics is enhanced by the Zr and Ti co-doping (Figs. 3e and f) [4,34–36]. For potential practical applications, single layers pouch cells with bare NCM811 and ZT-NCM811 cathodes and commercial graphite were assembled. As shown in Figs. 3g and h, the ZT-NCM811 shows a high discharge capacity of 180 mAh/g at 1C with improved capacity retention of 87.2% after 300 cycles, much higher than that of NCM811 (62.9% after 300 cycles). In addition, both samples have a high coulombic efficiency close to 100%. Therefore, the Zr and Ti co-doping can elevate the rapid charging/discharging capabilities and cycle durability, enlarging the application fields of NCM811 in commercial LIBs with high-energy density and long operation life.

To deeply understand the mechanism of the improved rate capabilities and cycling stability for ZT-NCM811 electrodes, dQ/dV profiles were calculated by differentiating the charging/discharging curves (Fig. S8 in Supporting information) of the NCM811 and ZT-NCM811 (Figs. 4a and b). Both cathodes undergo a series of phase transitions which is in accord with CV curves, and the H2-H3 phase transition of ZT-NCM811 hardly changed after 200 cycles, indicating the excellent reversibility. In comparison, the peaks of the NCM811 noticeably precipitate in intensity and become gradually polarized, which is due to the structural degradation during cycling [4,12]. The Nyquist plots and the corresponding equivalent circuit were exhibited in Figs. S9 and S10 (Supporting information), and the fitting results were shown in Figs. 4c and d. After 100 cycles, the Rct of ZT-NCM811 (94.2 Ω) is less than that of NCM811 (300.5 Ω), further implying the inhibition of the structure transformation from the layered phase to the electrochemically inactive rock salt phase resulting from more stable layered structure. The variation tendency of Rsf also manifests that Zr and Ti co-doping can mitigate side reactions of the electrode/electrolyte interface [37–40]. Furthermore, *in situ* differential electrochemical mass spectrometry (DEMS) was performed to detect the O_2 and CO_2 release during charge process for the NCM811 and ZT-NCM811(Figs. 4e and f). The lattice oxygen becomes more erratic along with the lithium extraction, and then the accompanying CO_2 released from the NCM811 due to the chemical oxidization reaction between the electrolyte and oxygen radicals [10]. Clearly, ZT-NCM811 has almost no gas evolution during the first charge cycle while NCM811 started to release O_2 after the H2 phase, demonstrating the high oxygen stability of ZT-NCM811 reinforced by stronger Zr-O and Ti-O bonds [5]. Consequently, Zr and Ti co-doping can elevate the reversibility of H2-H3 phase transition and strengthen the lattice oxygen stability simultaneously, resulting in ultra-indurative layered structure and excellent Li-ion diffusion.

To further probe the structural failure mechanism and the effect of Zr and Ti modification during long-term cycling, the structure and morphology of ZT-NCM811 and NCM811 after 100 cycles were analyzed by XRD, XPS, ICP and SEM. XRD patterns of ZT-NCM811 and NCM811 after 100 cycles were shown in Fig. 5a. The layered structure of ZT-NCM811 was well maintained after lithiation/delithiation process, and there are no extra peaks of the impurity phase except characteristic peaks of metallic aluminum. Contrastively, the $I_{(003)}/I_{(104)}$ ratio for the NCM811 critically decreases, indicating abundant Li^+ migrating from Li layers to TM layers [12,25]. Moreover, impurity phase was detected in XRD patterns of NCM811, which might originate from the structure transformation of layered oxides [13]. The Zr and Ti co-doping also has a positive effect on interfacial stability. The C 1s and F

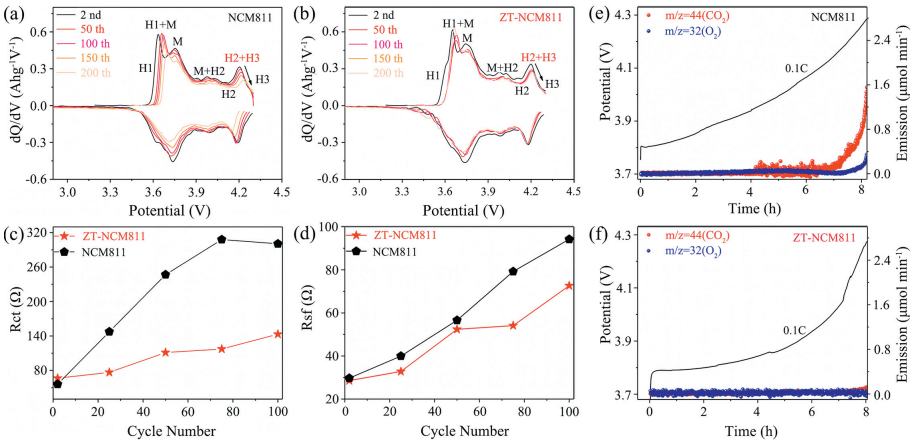

Fig. 4. (a, b) The calculated dQ/dV profiles by differentiating discharge/charge curves, (c) R_{ct} and (d) R_{sf} values at various cycles for NCM811 and ZT-NCM811. (e, f) Operando DEMS curves of NCM811 and ZT-NCM811 during the first charge process at 0.1 C.

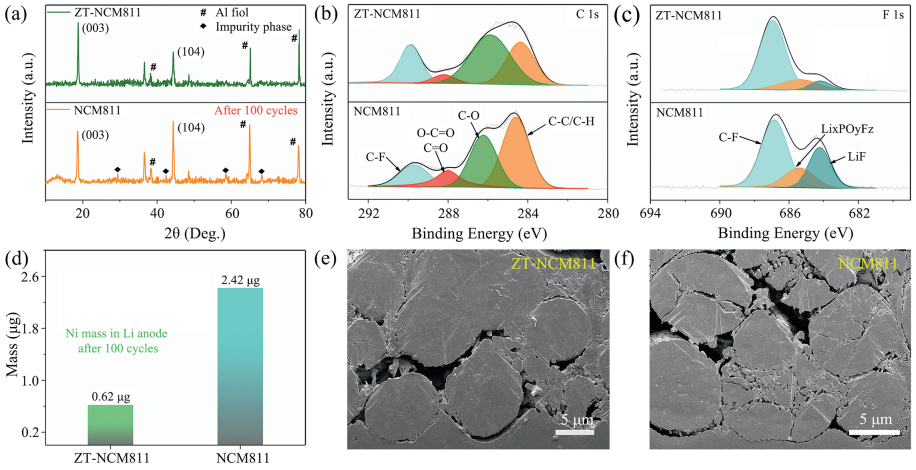

Fig. 5. (a) XRD patterns, (b) C 1s and (c) F 1s XPS spectra, (d) the amount of Ni deposited on the Li-anode, (e, f) cross-sectional SEM images of the ZT-NCM811 and NCM811 after 100 cycles.

1s XPS spectra of the ZT-NCM811 and NCM811 after cycling were depicted in Figs. 5b and c, the peaks in C 1s spectra at 284.6, 286.2, 288.0, and 289.7 eV are assigned to C-C/C-H species, C–O species, C=O/O–C=O species (the decomposition products of electrolyte), C-F groups of PVDF, respectively [33]. Strikingly, the peak intensity of C=O/O–C=O groups for NCM811 is higher than that of ZT-NCM811, indicating less interface parasitic reactions after Zr and Ti modification. For the F 1s region, the less $Li_xPO_yF_z$ and LiF which resulting from dissolved TM cations further evidence above point [12,38]. Meanwhile, the dissolved TM can migrate to the anode, damaging the solid-electrolyte interphase (SEI) and causing numerous active Li trapping, and lowering the capacity retention [41,42]. As shown in Fig. 5d, the Ni mass migrate to the Li anode of NCM811 after 100 cycles was 3.9 times higher than that of ZT-NCM811, which resulting from stronger interface stability strengthened by Zr and Ti doping. Ultimately, the spherical integrity of ZT-NCM811 was well maintained benefiting from the outstanding crystal texture and interface stability, whilst the distinct particle fracture are observed for the NCM811 after 100 cycles (Figs. 5e and f). SEM images of ZT-NCM811 and NCM811 after 100, 200, 300 cycles were also exhibited in Fig. S11 (Supporting information), it is noted that ZT-NCM811 has almost no cracked particles after 300 cycles, whilst NCM811 has increasingly cracked particles as the cycle number. Therefore, the co-doping strategy can suppress the pernicious phase transformation and interface parasitic reactions, resulting in the excellent rate capability and cycle durability.

In summary, the Zr/Ti dual-doped NCM811 cathode have been demonstrated, in which Zr-ion is doped into both TM layers and lithium layers and Ti-ion is only distributed in TM layers. After optimizing the doping content of each element, the ZT-NCM811 delivers a highest specific capacity of 212 mAh/g at 0.1 C and 124 mAh/g at 10 C, respectively, also much larger than the undoped and single-doped NCM811. A 98.8% of capacity retention at 1 C is achieved after 100 cycles. Even assembled into ZT-NCM811/graphite full cell, it equally exhibits superior battery performances and durability. Based on the various characterizations and in/ex-situ analysis, the reason is mainly ascribed to the following two aspects. One is that Zr-ion located at Li-slab can impede the abrupt shrinkage along c-axis with reduced Li/Ni disorder in charge process, retarding the phase transformation of NCM811 from layered structure to rock-salt phase. Another is that the robust Zr-O and Ti-O bonds stabilize the lattice oxygen and surface chemistry, and therefore greatly reducing the parasitic reactions with electrolyte. This finding may be of certain reference significance to clarify the coupling effects of multi-element doping and the corresponding performance enhancement mechanism.

Declaration of competing interest

The authors declare that they have no known competing financial interests or personal relationships that could have appeared to influence the work reported in this paper.

Acknowledgment

This work was supported by the National Natural Science Foundation of China (Nos. 21975074, 91834301), the Innovation Program of Shanghai Municipal Education Commission, and the Fundamental Research Funds for the Central Universities.

Supplementary materials

Supplementary material associated with this article can be found, in the online version, at doi:10.1016/j.cclet.2022.07.061.

References

[1] W. Li, E.M. Erickson, A. Manthiram, Nat. Energy 5 (2020) 26–34.
[2] S.S. Sharmaa, A. Manthiram, Energy Environ. Sci. 13 (2020) 4087–4097.
[3] Y. Hua, S. Zhou, H. Cui, et al., Int. J. Energy Res. 44 (2020) 11059–11087.
[4] H. Yu, Y. Cao, H. Jiang, et al., Nat. Commun. 12 (2021) 4564.
[5] M. Yoon, Y. Dong, J. Hwang, et al., Nat. Energy 6 (2021) 362–371.
[6] W. Liu, P. Oh, X. Liu, et al., Angew. Chem. Int. Ed. 54 (2015) 4440–4457.
[7] U.H. Kim, G.T. Park, B.K. Son, et al., Nat. Energy 5 (2020) 860–869.
[8] Y. Bi, J. Tao, Y. Wu, et al., Science 370 (2020) 1313–1317.
[9] W. Huang, W. Li, L. Wang, et al., Small 52 (2021) 2104282.
[10] C.H. Jung, D.H. Kim, D. Eum, et al., Adv. Funct. Mater. 18 (2021) 2010095.
[11] C.H. Jung, Q. Li, D.H. Kim, et al., Mater. Chem. 9 (2021) 17415–17424.
[12] H. Zhu, H. Yu, H. jiang, et al., Chem. Eng. Sci. 217 (2020) 115518.
[13] H. Yu, H. Zhu, H. Jiang, et al., Chem. Eng. J. 412 (2021) 128625.
[14] I.M. Markus, F. Lin, K.C. Kam, et al., J. Phys. Chem. Lett. 5 (2014) 3649–3655.
[15] S.J. Do, P. Santhoshkumar, S.H. Kang, et al., Ceramics International 6 (2019) 6972–6977.
[16] S. Gao, X. Zhan, Y.T. Cheng, J. Power Sources 411 (2019) 45–52.
[17] J.N. Zhang, Q. Li, C. Ouyang, et al., Nat. Energy 4 (2020) 594–603.
[18] L. Mu, R. Zhang, W.H. Kan, et al., Chem. Mater. 31 (2019) 9769–9776.
[19] Q. Liu, X. Su, D. Lei, et al., Nat. Energy 3 (2018) 936–943.
[20] S. Sivaprakash, S.B. Majumder, J. Alloy. Compd. 479 (2009) 561–568.
[21] F. Schipper, M. Dixit, D. Kovacheva, et al., J. Mater. Chem. A 4 (2016) 16073.
[22] Y. Xia, J. Zheng, C. Wang, M. Gu, Nano Energy 49 (2018) 434–452.
[23] A. Liu, N. Zhang, J.E. Stark, et al., J. Electrochem. Soc. 168 (2021) 040531.
[24] A. Liu, N. Zhang, J.E. Stark, et al., J. Electrochem. Soc. 168 (2021) 050506.
[25] Z. Chen, Z. Wang, G.T. Kim, et al., ACS Appl. Mater. Interfaces 11 (2019) 26994–27003.
[26] Q. Li, Z. Li, S. Wu, et al., ACS Appl. Energy Mater. 12 (2020) 11741–11751.
[27] J. Li, Y. Li, Y. Guo, et al., J. Mater. Sci. Mater. Electron. 29 (2018) 10702–10708.
[28] T. He, Y. Lu, Y. Su, et al., ChemSusChem 11 (2018) 1639–1648.
[29] D. Liu, S. Liu, C. Zhang, et al., ACS Sustainable Chem. Eng. 7 (2019) 10661–10669.
[30] Z. Yang, H. Yu, Y. Hu, H. Jiang, et al., Chem. Eng. Sci. 231 (2021) 116297.
[31] D. Wang, X. Li, Z. Wang, et al., Electrochim. Acta 188 (2016) 48–56.
[32] H. Yu, Y. Li, H. Jiang, et al., Ind. Eng. Chem. Res. 58 (2019) 4108–4115.
[33] F. Wu, S. Fang, M. Kuenzel, et al., Joule 5 (2021) 1–18.
[34] Z. Deng, H. Jiang, Y. Hu, et al., Adv. Mater. 29 (2017) 1603020.
[35] H. Yu, S. Wang, Y. Hu, et al., Green Energy Environ. 7 (2022) 266–274.
[36] W. Li, J. Zhang, Y. Zhou, et al., ACS Appl. Mater. Interfaces 12 (2020) 47513–47525.
[37] K. Ma, Y. Liu, H. Jiang, et al., CCS Chem. 2 (2020) 1472–1482.
[38] J. Li, W. Li, S. Wang, et al., Chem. Mater. 30 (2018) 3101–3109.
[39] Changhao Wang, Yahao Li, Feng Cao, et al., ACS Appl. Mater. Interface 14 (2022) 10457–10466.
[40] Xinyi Shan, Yu Zhong, Lingjie Zhang, et al., J. Phys. Chem. C 125 (2021) 19060–19080.
[41] W. Li, U.H. Kim, A. Dolocan, Y.K. Sun, A. Manthiram, ACS Nano 11 (2017) 5853–5863.
[42] W. Li, A. Dolocan, P. Oh, et al., Nat. Commun. 8 (2017) 1458.